

Radio-frequency assisted switching in perpendicular magnetic tunnel junctions

Mark Hayward¹, Salvatore Perna², Massimiliano d'Aquino², Claudio Serpico²,
Wonjoon Jung³, Chunhui Dai^{3†}, Patrick M. Braganca³, and Ilya N. Krivorotov^{1,*}

¹ *Department of Physics and Astronomy, University of California, Irvine, California, 92697, USA*

² *Department of Electrical Engineering and Information Technology,
University of Naples Federico II, Naples, Italy. and*

³ *Western Digital Technologies, San Jose, California, 95119, USA*

Spin-transfer torque magnetic random-access memory (STT-MRAM) relies on nanoscale magnetic tunnel junctions (MTJs) as its fundamental building blocks. Next-generation STT-MRAM requires strategies that simultaneously improve switching energy efficiency and device endurance. Here, we present the first study of perpendicular STT-MRAM writing assisted by radio-frequency (RF) spin torque. We show that applying a small-amplitude RF pulse prior to a direct-current (DC) writing pulse enhances the MTJ switching probability, with the efficiency gain increasing at lower RF frequencies. This RF+DC writing scheme enables shorter DC pulses, thereby improving device endurance. Analytical and numerical modeling qualitatively reproduces the experimental trends, while quantitative discrepancies indicate that realistic MTJ properties beyond idealized models play an important role in RF-assisted switching.

Introduction

STT-MRAM is a leading candidate for next-generation nonvolatile memory, combining sub-nanosecond switching [1–5], CMOS compatibility [6–9], scalability to future technology nodes [10], and radiation hardness [11]. Significant progress has been made toward commercialization, yet the technology is currently limited to niche applications [12]. Advancing the technology to mainstream implementation requires overcoming the key challenges of relatively low energy efficiency, high write current density, and limited endurance [8]. In perpendicular MTJs (p-MTJs), which constitute the core of contemporary STT-MRAM, the write current density must be kept high enough to guarantee reliable switching, but this comes at the cost of increased power consumption and the risk of tunnel barrier breakdown [13]. Scaling the MTJ size below 20 nm further exacerbates this tradeoff by making the thermal stability and write reliability harder to balance [14].

The relatively high voltage pulses applied during the write operation accelerate degradation of the ultrathin MgO barrier, leading to reduced device lifetimes. This reliability challenge stresses the need for writing schemes that deliver switching at reduced voltage levels, without compromising retention or write error rates. An alternative, spin-orbit torque MRAM (SOT-MRAM), addresses the problem of dielectric breakdown by separating the read and write current paths [15–21]. Although this decoupling enables fast switching without stressing the MgO barrier, the three-terminal geometry of SOT-MRAM imposes a large footprint that constrains storage density and integration. Therefore, innovation in the engineering of the STT-MRAM stack, device design, and write protocols is crucial for the development of energy-efficient STT-MRAM.

A straightforward strategy to reduce the write voltage in STT-MRAM is to increase the duration of the DC write pulse. However, this approach relying on thermally-assisted switching comes at the cost of higher write energy and reduced energy efficiency [22–24]. The tradeoff between the write voltage amplitude and energy efficiency motivates the search for alternative write schemes [25] that achieve reliable switching without compromising endurance or efficiency.

An attractive approach is to combine the DC write pulse with an RF current pulse [26–28] – a method inspired by studies of microwave-assisted magnetization reversal in magnetic media [29–34]. This RF-assisted strategy has previously been studied in in-plane MTJs and in all-metallic spin valves, where an enhanced switching probability was observed when the RF drive frequency was tuned to the ferromagnetic resonance (FMR) of the free layer (FL) [35, 36]. In thermally unstable, superparamagnetic in-plane MTJs, a strong enhancement of random telegraph switching has been demonstrated at sub-GHz frequencies, where RF excitation drives low-dimensional chaotic dynamics of the FL [37].

Despite these promising results, RF-assisted switching [38, 39] in p-MTJs forming the basis of modern STT-MRAM technology has only been studied for RF frequencies near FMR [40]. In this work, we report experimental and theoretical studies of RF-assisted switching in thermally stable p-MTJs over a broad RF frequency range. We show that a small-amplitude RF pulse applied just before the DC write pulse can significantly increase the switching probability. This RF+DC writing protocol enables a reduction of the DC pulse duration, thereby improving device endurance.

Furthermore, we find that the efficiency of RF assistance increases as the RF frequency is reduced. This is a notable technological advantage, since implementing sub-GHz RF drive circuitry in CMOS is simpler and more cost-effective than realizing GHz-frequency sources required for the FMR-frequency operation. We present measurements of RF-assisted switching across multi-

* Corresponding author email: ilya.krivorotov@uci.edu

† Current address: Samsung Semiconductor Inc, 3655 N. First Street, San Jose, CA 95134, USA

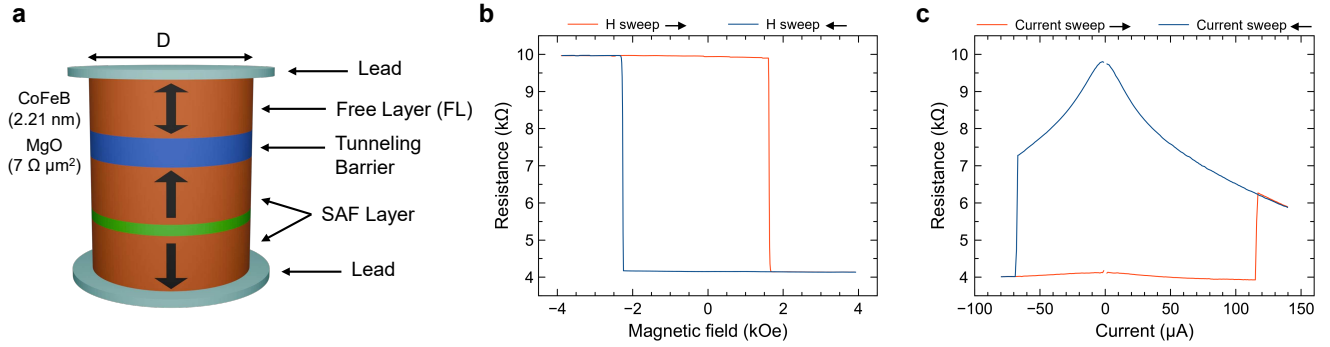


FIG. 1. **Device schematics and switching characteristics of a p-MTJ.** **a** Schematic of a circular, nanoscale p-MTJ of diameter D consisting of an SAF reference layer and a 2.21 nm thick CoFeB FL separated by an MgO tunnel barrier with a resistance-area product of $7 \Omega \mu\text{m}^2$. Magnetic field **b** and current **c** hysteresis loops for a $D = 45 \text{ nm}$ p-MTJ.

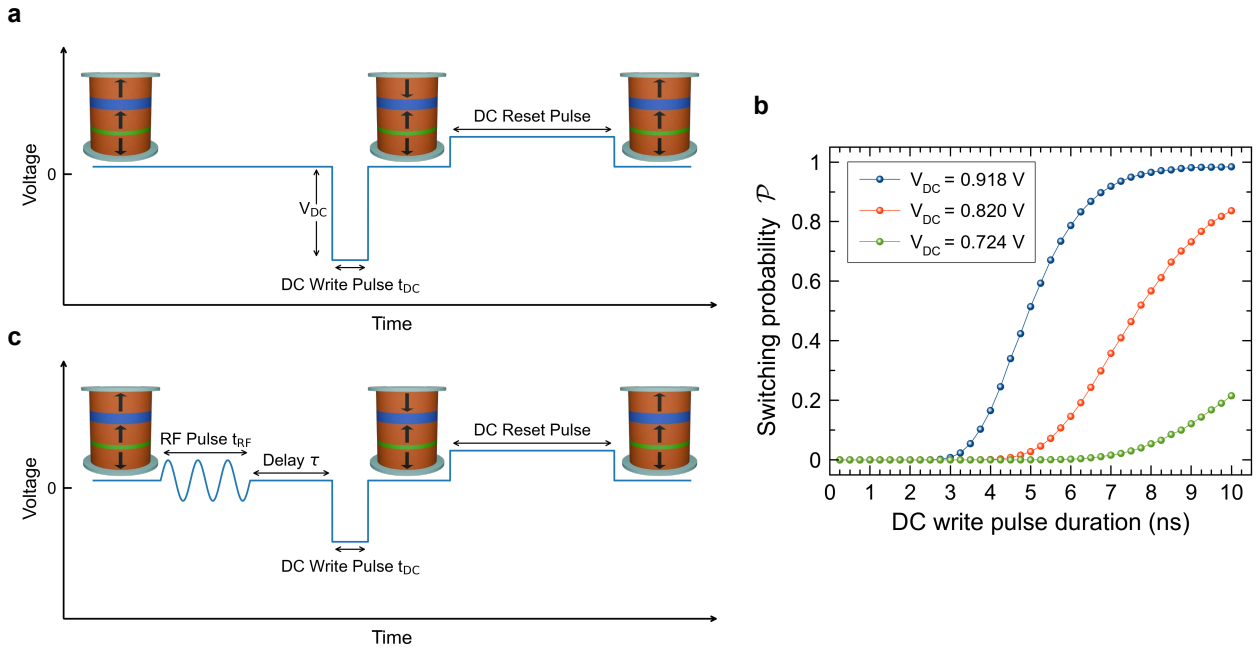


FIG. 2. **Waveforms for current-induced p-MTJ switching.** **a** The waveform used for measurements of p-MTJ switching probability \mathcal{P} in the conventional DC write pulse switching regime. **b** \mathcal{P} as a function of DC pulse duration t_{DC} for three pulse amplitudes measured using the pulse sequence in **a** for a $D = 45 \text{ nm}$ device. **c** The waveform used for measurements of RF-assisted switching.

ple p-MTJ diameters and compare these experimental results to an analytical model and numerical simulations.

Experiment

We investigate RF-assisted switching in circular nanoscale p-MTJs, schematically shown in Fig. 1a. The devices studied have diameters $D = 85, 65, 45,$ and 25 nm , a CoFeB FL thickness $d = 2.21 \text{ nm}$, and an

MgO tunneling barrier with resistance-area product of $7 \Omega \mu\text{m}^2$. The pinned layer is a synthetic antiferromagnet (SAF) [41] (Methods). Figure 1b,c show measurements of resistance as a function of out-of-plane magnetic field and quasi-static current for a $D = 45 \text{ nm}$ p-MTJ. These measurements demonstrate the thermal stability and high tunneling magnetoresistance of the device.

Figure 2a illustrates the pulse sequence used for mea-

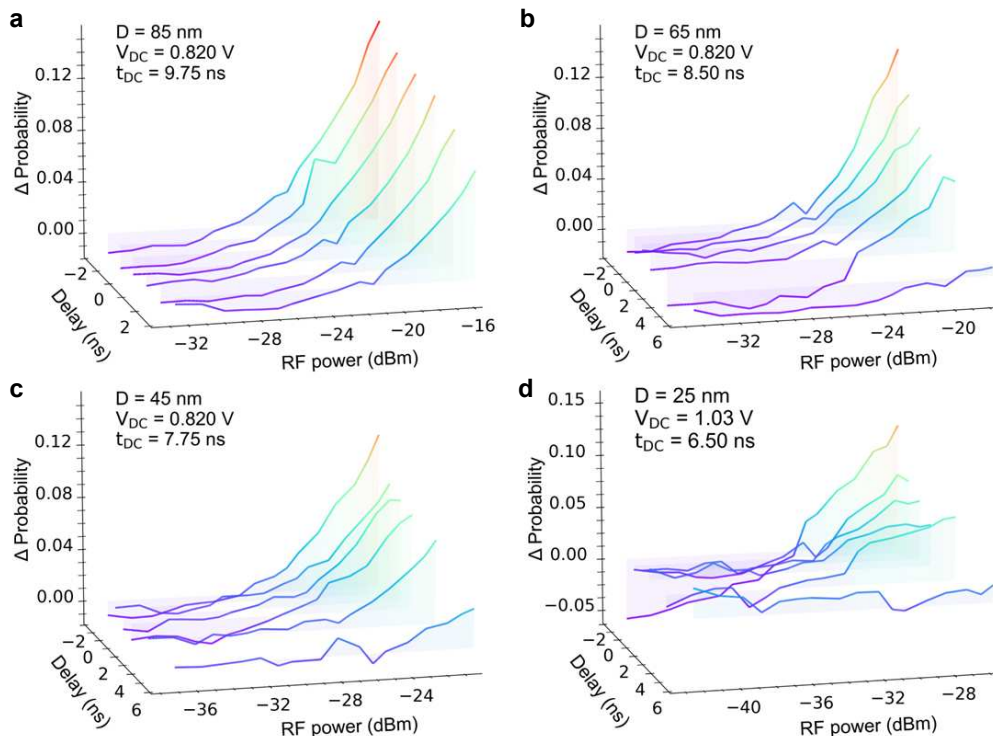


FIG. 3. **RF-assisted increase in switching probability $\Delta\mathcal{P}$ versus RF power P_{RF} and RF-DC delay τ .** In these measurements, the RF pulse frequency $f_{\text{RF}} = 0.1$ GHz, and duration $t_{\text{RF}} = 30$ ns are fixed. The DC write pulse parameters for each p-MTJ are adjusted to achieve $\mathcal{P} = 0.5$ in the absence of the RF pulse. Four p-MTJ diameters are studied: **a** $D = 85$ nm, **b** $D = 65$ nm, **c** $D = 45$ nm, and **d** $D = 25$ nm.

measurements of p-MTJ switching probability \mathcal{P} ($0 \leq \mathcal{P} \leq 1$) in the conventional DC write pulse switching regime. In this paper, we study switching from the low-resistance parallel (P) to the high-resistance antiparallel (AP) state at room temperature in zero external magnetic field. A large-amplitude square DC write pulse is applied to the device in the P state, followed by the resultant resistance readout and a longer reset pulse returning the MTJ back to the initial P state. The measurement is repeated 10^5 times to reliably measure \mathcal{P} for a given write pulse duration t_{DC} and amplitude V_{DC} . Figure 2b shows the results of our measurements for a $D = 45$ nm device as a function of t_{DC} for three values of V_{DC} . All voltage values reported in this paper are voltages applied across the MTJ (Supplementary Note 1).

For studies of RF-assisted switching, the DC write pulse is preceded by an RF pulse of duration t_{RF} , frequency f_{RF} and root mean square (RMS) amplitude V_{RF} as shown in Fig. 2c. A variable delay τ is introduced between the end of the RF pulse and the onset of the DC pulse; negative delay $\tau < 0$ corresponds to temporal overlap of the RF and DC pulses. We study both the $\tau \geq 0$ and $\tau < 0$ regimes of RF-assisted switching. The phase of the RF pulse in our measurements is random (Supplementary Note 1 and Supplementary Figure S1).

For these measurements, we first select the values of V_{DC} and t_{DC} that give $\mathcal{P} = 0.5$ in the absence of an

RF pulse as determined from the type of data in Fig. 2b for each device. We then add an RF pulse with $t_{\text{RF}} > t_{\text{DC}}$ before the DC pulse and measure the increase in the switching probability $\Delta\mathcal{P}$ above the $\mathcal{P} = 0.5$ baseline.

Figure 3 shows $\Delta\mathcal{P}$ measured as a function of RF power P_{RF} and delay τ for four device diameters. In these measurements, $f_{\text{RF}} = 0.1$ GHz, $t_{\text{RF}} = 30$ ns, and P_{RF} in dBm is defined as the power dissipated by the sample during the RF pulse:

$$P_{\text{RF}} = 10 \cdot \log_{10} \left(\frac{V_{\text{RF}}^2}{R_{\text{P}}} \cdot \frac{1}{1 \text{ mW}} \right), \quad (1)$$

where R_{P} is the P state resistance (Supplementary Note 1).

We also study the effect of time delay between the RF and DC write pulses on $\Delta\mathcal{P}$. Figure 4 shows the dependence of $\Delta\mathcal{P}$ on τ at $V_{\text{RF}} = 0.195$ V for four MTJ diameters. $\Delta\mathcal{P}$ monotonically increases with decreasing τ and is generally positive in both the $\tau \geq 0$ and $\tau < 0$ regimes. For $\tau = -7$ ns, $\Delta\mathcal{P}$ is 0.31, 0.24, 0.27 and 0.15 for the $D = 85, 65, 45,$ and 25 nm devices, respectively. While at $\tau = 0$, $\Delta\mathcal{P}$ is 0.13, 0.08, 0.08 and 0.06 for the $D = 85, 65, 45,$ and 25 nm devices, respectively.

Figure 5 shows the dependence of $\Delta\mathcal{P}$ on f_{RF} for the $D = 45$ nm device at $P_{\text{RF}} = -21$ dBm and $\tau = -2$ ns. These data, taken at frequencies well below the FL

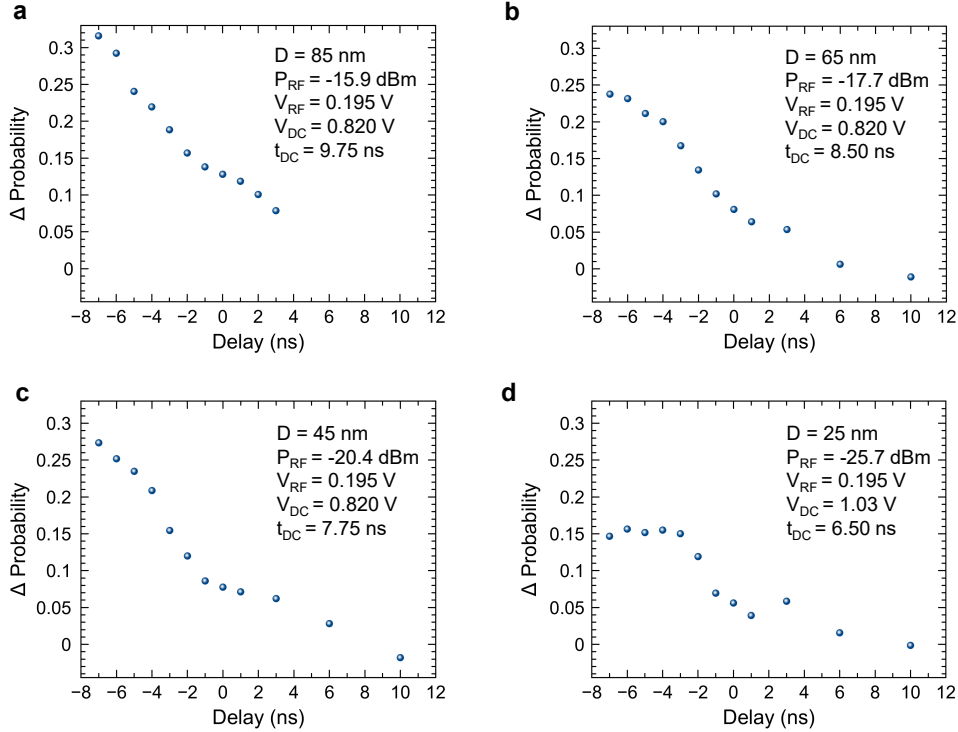


FIG. 4. **RF-assisted increase in switching probability $\Delta\mathcal{P}$ as a function of the RF-DC delay τ at $V_{\text{RF}} = 0.195$ V.** Four p-MTJ diameters are studied: **a** $D = 85$ nm. **b** $D = 65$ nm. **c** $D = 45$ nm. **d** $D = 25$ nm.

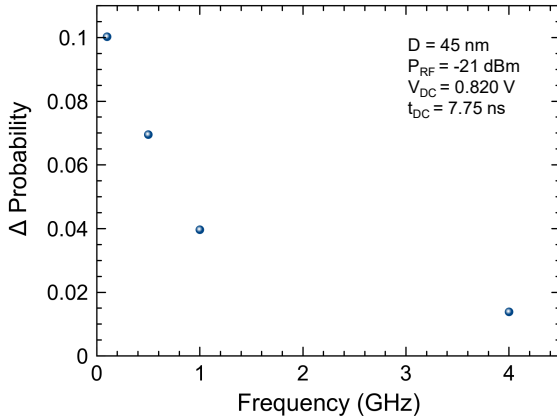


FIG. 5. **RF-assisted increase in switching probability $\Delta\mathcal{P}$ as a function of RF frequency.**

FMR frequency (12 GHz, Supplementary Note 2), reveal that RF-assisted switching becomes more efficient with decreasing RF frequency. A qualitatively similar dependence of $\Delta\mathcal{P}$ on f_{RF} is observed in the $\tau \geq 0$ regime.

Theory

In order to understand the mechanisms of the experimentally observed RF-assisted switching, we made room-temperature ($T = 300$ K) numerical macrospin and mi-

cro-magnetic simulations of the switching process. Simulations were made for all the MTJ diameters considered in the experiments (Supplementary Note 3). Here we show the results for the device with $D = 45$ nm. Simulations of an ensemble of multiple replicas were performed to compute the switching probability. The magnetization dynamics of each replica were computed using both micromagnetic and macrospin solvers (see Supplementary Note 3). For the micromagnetic analysis, 10^2 replicas were simulated, while for the macrospin simulations 10^4 replicas were used. The switching probability was then determined by counting the number of replicas that showed P to AP switching.

For these simulations, we first select the values of V_{DC} and t_{DC} that produce $\mathcal{P} = 0.5$ in the absence of an RF pulse for each device. We then add an RF pulse preceding the DC pulse and calculate the increase in the switching probability $\Delta\mathcal{P}$ above the $\mathcal{P} = 0.5$ baseline. Figure 6 shows the simulated $\Delta\mathcal{P}$ due to the RF pulse assist versus normalized RF power \hat{P}_{RF} and delay τ between the RF and DC write pulses. The RF power is normalized to the minimal theoretical power required to switch the magnetic state with a DC current in the absence of thermal fluctuations ($T = 0$ K) [42]. This minimal power is analytically calculated in the macrospin approximation for the values of the FL dimensions, the uniaxial magnetocrystalline anisotropy constant K_{AN} , saturation magnetization M_s , and Gilbert damping constant α given in

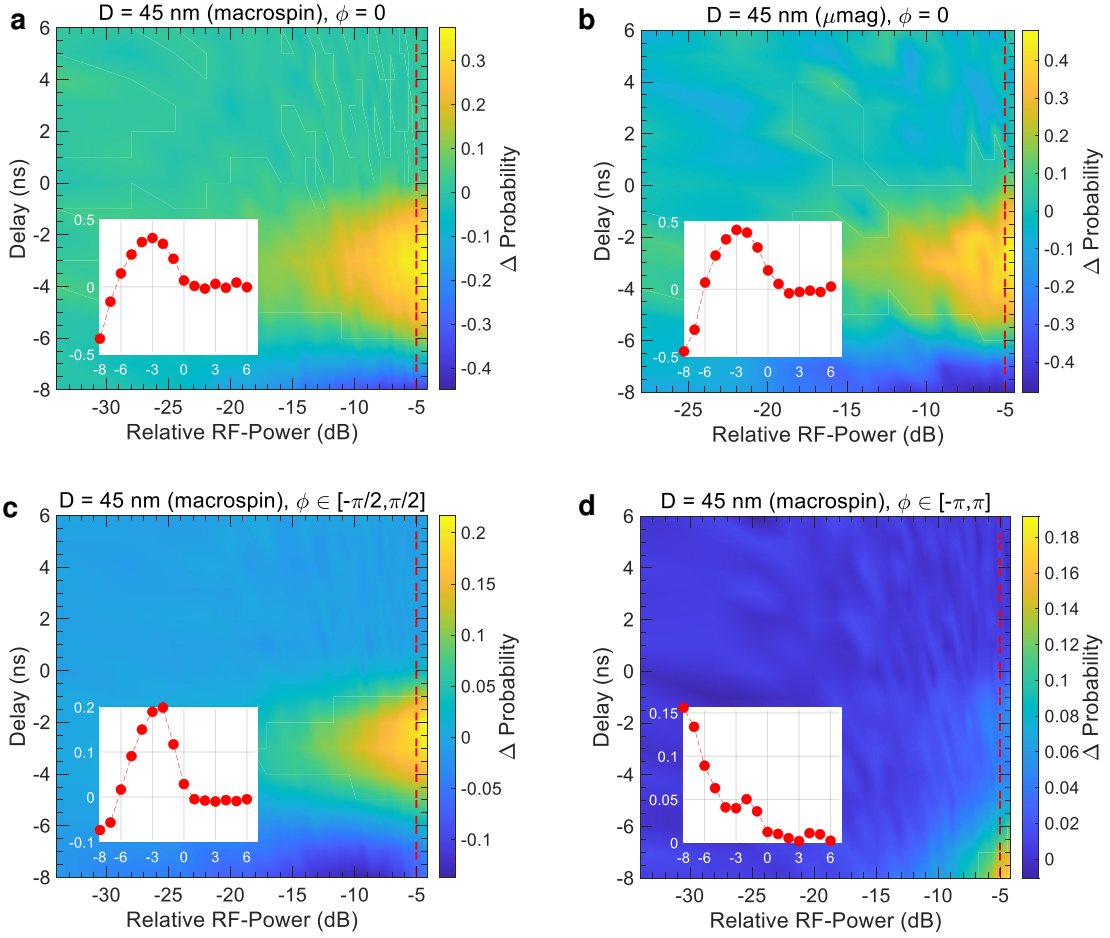


FIG. 6. **Simulations of $\Delta\mathcal{P}$ as a function of normalized RF power \tilde{P}_{RF} and RF-DC delay τ .** $\Delta\mathcal{P}$ is represented by the color scale, and the insets show $\Delta\mathcal{P}$ versus τ at $\tilde{P}_{\text{RF}} = -5$ dB. In these simulations, $f_{\text{RF}} = 0.1$ GHz and $t_{\text{RF}} = 30$ ns. **a** Macrospin simulations with the RF phase constant $\phi = 0$. **b** Micromagnetic simulations with $\phi = 0$. **c** Macrospin simulations with ϕ uniformly distributed over $[-\pi/2, \pi/2]$. **d** Macrospin simulations with ϕ uniformly distributed over $[-\pi, \pi]$.

Table I of Methods. Figure 6a shows macrospin $\Delta\mathcal{P}$ as a function of \tilde{P}_{RF} and τ when the phase constant ϕ of the RF voltage $\sqrt{2}V_{\text{RF}} \cos(\omega_{\text{RF}}t + \phi)$ is set to zero. Notice that $t = 0$ corresponds to the time instant where the DC pulse is applied and $\omega_{\text{RF}} = 2\pi f_{\text{RF}}$. These results are significantly different from the experiment in Fig. 3c and Fig. 4c. This is most clearly seen from the comparison of the inset in Fig. 6a showing $\Delta\mathcal{P}$ versus τ at $\tilde{P}_{\text{RF}} = -5$ dB and the experimental data in Fig. 4c. Indeed, the measured $\Delta\mathcal{P}$ is a monotonically decreasing function of τ , while the simulated $\Delta\mathcal{P}(\tau)$ has a peak at $\tau = -3$ ns. The micromagnetic results in Fig. 6b are similar to the macrospin with a slightly enhanced $\Delta\mathcal{P}$. The number of replicas in the macrospin simulations is large enough to yield a $\sim 1\%$ error in $\Delta\mathcal{P}$ while the micromagnetic results are precise within $\sim 10\%$.

The discrepancy with the experiment is expected because the simulations assume a fixed phase $\phi = 0$, while the measurements average over random phases. To address this discrepancy, we performed macrospin simulations with ϕ uniformly distributed over $[-\pi/2, \pi/2]$

(Fig. 6c) and $[-\pi, \pi]$ (Fig. 6d) intervals, the latter directly mimicking the experimental conditions. The inset in Fig. 6d is qualitatively similar to the corresponding experimental results in Fig. 4c, although quantitative discrepancies remain. Similar results were obtained for devices with other studied MTJ diameters (Supplementary Note 3 and Supplementary Figure S3).

The numerically calculated dependence of $\Delta\mathcal{P}$ on \tilde{P}_{RF} and τ can be further elucidated by analytical modeling in the framework of damping-switching dynamics [43, 44]. This analytical model makes five assumptions:

- (i) macrospin approximation.
- (ii) prior to the RF+DC waveform, the distribution of replicas is assumed to be described by the Néel-Brown model [45] in the high-energy-barrier case. Therefore, the initial probability density function (PDF) of the replicas $p_0(m_z)$ is given by the following expression:

$$p_0(m_z) = \frac{1}{Z} \exp\left(\frac{k_{\text{eff}}}{2T} m_z^2\right), \quad m_z \in [0, 1], \quad (2)$$

where

$$Z = \int_0^1 \exp\left(\frac{k_{\text{eff}}}{2\tilde{T}} m_z^2\right) dm_z = \sqrt{\frac{\pi\tilde{T}}{2k_{\text{eff}}}} \operatorname{erfi}\left(\sqrt{\frac{k_{\text{eff}}}{2\tilde{T}}}\right) \quad (3)$$

is the partition function, m_z is the out-of-plane component of the FL magnetization unit vector $\mathbf{m} = \mathbf{M}/M_s(T)$, with $M_s(T)$ the saturation magnetization at a certain temperature T , and $\operatorname{erfi}(\cdot)$ is the imaginary error function. k_{eff} is the normalized effective magnetic anisotropy constant of the FL given by $k_{\text{eff}} = 2K_{\text{AN}}/(\mu_0 M_s^2) - (D_z - D_{\perp})$. Here, K_{AN} is the uniaxial

magnetocrystalline anisotropy constant in SI units, D_z and D_{\perp} are the demagnetizing factors along the symmetry axis and the perpendicular direction ($2D_{\perp} + D_z = 1$), and μ_0 is the vacuum magnetic permeability. $\tilde{T} = k_B T/(\mu_0 M_s^2 V)$ is the normalized temperature, where k_B is the Boltzmann constant and V is the FL volume.

(iii) magnetization dynamics is governed by the deterministic Landau-Lifshitz-Gilbert (LLG) equation.

(iv) for $\tau > 0$, the RF pulse does not affect the switching probability.

(v) for $\tau < 0$, the RF+DC waveform is replaced by an effective DC pulse of duration t_{DC} and amplitude \bar{V}_{ST} :

$$\bar{V}_{\text{ST}} = V_{\text{DC}} + \frac{\sqrt{2}V_{\text{RF}}}{\omega_{\text{RF}}t_{\text{DC}}} \left[\sin(\omega_{\text{RF}}(t_{\text{RF}} - \tau) + \phi) - \sin(\omega_{\text{RF}}t_{\text{RF}} + \phi) \right], \quad (4)$$

which is V_{DC} plus the average RF voltage over the duration of the DC pulse, with t_{RF} the duration of the RF pulse. The theoretical foundations of these five assumptions are discussed in Supplementary Note 3.

The PDF of the FL magnetization at a time t is:

$$p(m_z, t) = \int_0^1 p_0(m_{z0}) p(m_z, t|m_{z0}, 0) dm_{z0}, \quad (5)$$

where m_{z0} is m_z at $t = 0$, which marks the onset of the \bar{V}_{ST} write pulse.

The magnetization switching dynamics is a damping-switching process in a uniaxial, bistable magnet between the two stable states $m_z = \pm 1$. In this case the magnetization trajectory from m_{z0} to m_z under the action of $\bar{H} = \bar{V}_{\text{ST}}/V_{c0} = \bar{\beta}_{\text{ST}}/(\alpha k_{\text{eff}})$ can be expressed in closed form by the following [44]: $q(m_z, m_{z0}, \bar{H}) = \alpha k_{\text{eff}} t$. The quantity \bar{H} is the effective DC voltage pulse amplitude normalized to V_{c0} , which is the critical DC voltage for switching at $T = 0$. For the numerical integration of the magnetization dynamics, the dimensionless LLG equation is considered [43]. Within it, the dimensionless volt-

age is β_{ST} , while the dimensionless critical voltage at zero temperature is given by αk_{eff} .

Solving the relation defining q for m_z , we obtain: $m_z(t) = \mu_z(m_{z0}, t, \bar{H})$, which allows us to rewrite Eq. (5) in the following form:

$$p(m_z, t) = \frac{p_0(\mu_z^{-1}(m_z))}{\lambda_z(m_z)}, \quad (6)$$

where $\lambda_z = d\mu_z/dm_{z0}$.

We assume that the FL switches if m_z changes sign compared to m_{z0} after the write pulse. Starting with the initial distribution with $m_{z0} > 0$, the switching probability can be computed by integrating the PDF over the range $m_z \in [-1, 0]$ that defines the well of the switched magnetic state $m_z = -1$. Such a state cannot be reached by a deterministic dynamics in a time window of finite duration. The closest state to $m_z = -1$ reachable in a finite time window is $m_z = \mu_z(0, t, \bar{H})$, which is the final state of a deterministic trajectory in the time interval $[0, t]$ starting from the initial state $m_z(0) = 0$. With these considerations, the switching probability \mathcal{P} at t is given by:

$$\mathcal{P}(t) = \int_{\mu_z(0, t, \bar{H})}^0 p(m_z, t) dm_z = \int_0^{\mu_z^{-1}(0, t, \bar{H})} p_0(m_{z0}) dm_{z0} = \frac{\operatorname{erfi}\left(\sqrt{\frac{k_{\text{eff}}}{2\tilde{T}}}\mu_z^{-1}(0, t, \bar{H})\right)}{\operatorname{erfi}\left(\sqrt{\frac{k_{\text{eff}}}{2\tilde{T}}}\right)}. \quad (7)$$

Taking into account that PDF depends on ϕ via \bar{H} , the

switching probability for ϕ uniformly distributed over the experimentally relevant interval $[-\pi, \pi]$ is:

$$P(t) = \frac{1}{2\pi \operatorname{erfi}\left(\sqrt{\frac{k_{\text{eff}}}{2\tilde{T}}}\right)} \int_0^{2\pi} \operatorname{erfi}\left(\sqrt{\frac{k_{\text{eff}}}{2\tilde{T}}}\mu_z^{-1}(0, t, \bar{H})\right) d\phi. \quad (8)$$

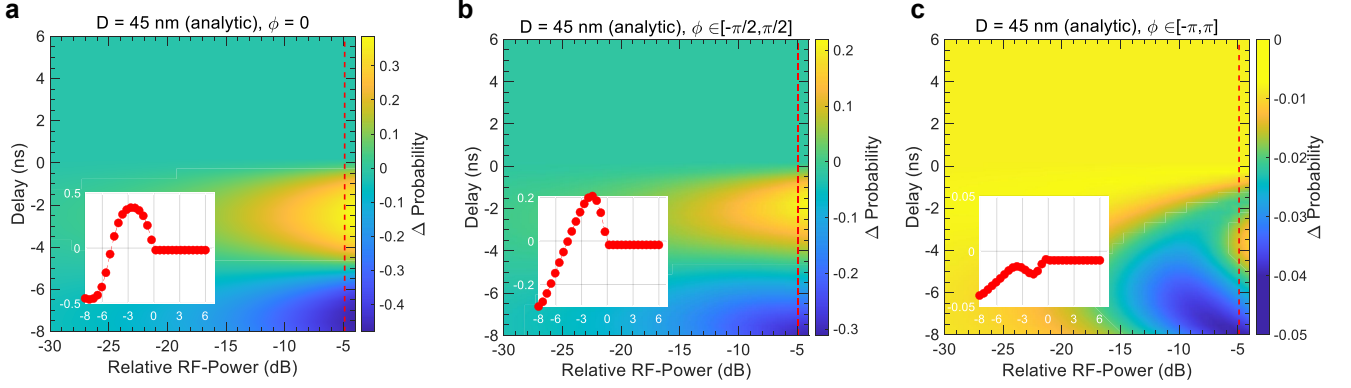


FIG. 7. Analytic model predictions of $\Delta\mathcal{P}$ as a function of normalized RF power \tilde{P}_{RF} and RF-DC delay τ . **a** $\phi = 0$. **b** ϕ uniformly distributed over $[-\pi/2, \pi/2]$. **c** ϕ uniformly distributed over $[-\pi, \pi]$.

In Fig. 7, we use Eq. (7) and Eq. (8) to compute $\Delta\mathcal{P}$ for the same parameters as numerical results in Fig. 6. In the case of $\phi = 0$ and $\phi \in [-\pi/2, \pi/2]$ (Fig. 7a,b), the agreement with the numerical results is quantitative, but its quality becomes worse for large values of P_{RF} and $\tau < 0$, where the analytical results underestimate $\Delta\mathcal{P}$. Since the effective write pulse amplitude \bar{V}_{ST} is an oscillatory function of τ , P_{RF} oscillates between positive and negative values for $\tau < 0$.

In the case of the fully random phase ϕ distributed in $\phi \in [-\pi, \pi]$ (Fig. 7c), analytical calculations do not predict an increase in \mathcal{P} , while numerical simulations show $\Delta\mathcal{P} > 0$ for large values of P_{RF} and $\tau < 0$. This is because $\mathcal{P}(\phi)$ in Eq. (7) is a periodic function of ϕ , and the enhancement of \mathcal{P} achieved for a given ϕ^* is approximately canceled by the reduction of \mathcal{P} for the phase $\phi^* + \pi$. Although this cancellation is not exact, $\Delta\mathcal{P}$ resulting from the averaging in ϕ is small ~ 0.01 .

In numerical simulations with sufficiently high \tilde{P}_{RF} and $\tau < 0$, $\Delta\mathcal{P}$ is not negligibly small because a larger number of switching events with respect to those predicted by the analytical model occur in the time interval where the RF pulse adds constructively to the DC pulse voltage. This fact is not surprising since the assumption (v) of the analytical model does not hold anymore (Supplemental Note 3). As a result, numerical simulations produce higher $\Delta\mathcal{P}$ than the analytical model.

Discussion

Figure 3 reveals that RF-assisted switching enhancement is observed for both positive and negative delays τ between the RF and DC pulses. The enhancement for $\tau < 0$ can be expected because the overlap between the RF and DC pulses can result in the net applied voltage exceeding V_{DC} in an interval of the combined RF+DC waveform. However, the RF-enhanced switching in the $\tau \geq 0$ regime is surprising. This latter regime is also important from a practical point of view because the combined RF+DC waveform voltage never exceeds V_{DC} ,

leading to enhanced switching without extra stress on the junction. From another angle, introduction of an RF pulse allows one to reduce the DC pulse duration t_{DC} for a targeted switching probability compared to the DC-only protocol. Since longer DC write pulses are known to stress the MTJ barrier oxide and reduce device endurance [46, 47], the RF+DC switching protocol in the $\tau \geq 0$ regime studied here is expected to enhance STT-MRAM endurance.

The maximum RF pulse amplitude used in this study, $V_{\text{RF}} = 0.195$ V, is much smaller than the DC write pulse amplitude ~ 1 V. Therefore, in the $\tau \geq 0$ regime, this small-amplitude RF assist does not diminish device endurance and only marginally increases the write energy while increasing the switching probability. This makes RF assist at $\tau = 0$ a viable strategy for an improved STT-MRAM write protocol.

Figure 3 also demonstrates that the small-amplitude RF pulse increases the switching probability for all device sizes down to $D = 25$ nm. This is promising for scalability of the RF+DC write. While the observed enhancement of switching probability $\Delta\mathcal{P}$ at $V_{\text{RF}} = 0.195$ V is smaller for the 25 nm device compared to the 85 nm device, the RF power dissipated by the 25 nm device at this RF assist voltage is 10 dB lower due to the higher resistance of the smaller MTJ. The effectiveness of the RF assist for all device sizes indicates that micromagnetic effects expected to be more pronounced in the larger devices do not play a crucial role in the observed effect. This is corroborated by our theoretical results in Fig. 6 revealing similar impact of the RF assist in the macrospin and micromagnetic approximations.

In principle, ohmic heating induced by the RF pulse could contribute to the enhancement of switching probability $\Delta\mathcal{P}$. However, because ohmic heating is frequency independent, it cannot account for the strong frequency dependence seen in Fig. 5. Circuit calibrations used in our experiments ensured uniform RF pulse power across all frequencies. If heating were the dominant mechanism,

the observed switching enhancement would be comparable across all frequencies at constant power. The strong frequency dependence of the RF assist demonstrated in Fig. 5 therefore eliminates ohmic heating of the MTJ by the RF pulse as a possible mechanism of the observed RF-induced switching enhancement [48].

Our theoretical predictions of RF-assisted switching in Fig. 6d are qualitatively similar to the experimental results in Fig. 3c and Fig. 4c. The theory captures the threshold character of the effect in the RF power and the observed decrease in the switching probability with the delay time τ between the RF and DC pulses. However, there are two quantitative differences. First, the theoretical threshold power is higher than the experimental one. Second, theoretical results shown in the insets of Fig. 6 suggest that the effect vanishes for delay times τ exceeding ~ 1 ns, while the observed effect in Fig. 4 persists up to $\tau \approx 6$ ns.

The theoretically predicted ~ 1 ns time scale is reasonable because it is similar to the characteristic magnetic energy relaxation time of the FL $\tau_E = 1/(4\pi\alpha f_{\text{FMR}}) = 0.66$ ns, where $\alpha = 0.0097$ and $f_{\text{FMR}} = 12$ GHz as determined by spin torque FMR measurements (Supplementary Note 2). For $\tau \gg \tau_E$, all magnetic energy added to the FL magnetization by the RF pulse is expected to dissipate away, and thus magnetization dynamics driven by the DC pulse is expected to be unaffected by the RF pulse. The observation of RF assist effects for $\tau \gg \tau_E$ suggests that, in addition to FMR dynamics, the FL also supports significantly slower magnetic dynamics.

Signatures of such slow magnetic dynamics have been previously observed in a different experiment [49] and were attributed to regions at the FL/MgO interface with reduced magnetization and weak exchange coupling. Our data in Fig. 4 provide additional support for this hypothesis of slow dynamics in the FL of a p-MTJ. Moreover, the greater enhancement of switching probability $\Delta\mathcal{P}$ at lower RF frequencies as shown in Fig. 5 suggests these dynamics are more efficiently excited at lower frequencies. This effect may be rooted in the structural, chemical, and magnetic inhomogeneity of the ultrathin CoFeB FL found in MTJ devices [50]. Electrical transport, FMR and magnetometry studies on ultrathin films and MTJ nanopillars based on Ta/CoFeB/MgO multilayers suggest that iron-based magnetic oxides form at the CoFeB/MgO interface [50, 51]. These slow magnetic dynamics attributed to the FL inhomogeneity could contribute to the enhancement of switching probability $\Delta\mathcal{P}$ for $\tau \geq 0$ but are beyond the scope of the theoretical framework of this paper.

The threshold character of the RF-induced enhancement of switching in Fig. 3 suggests the importance of nonlinear magneto-dynamics [52] for the RF assist. Both the threshold character of the RF assist in the RF power and the frequency dependence of its efficiency in Fig. 5 are consistent with the prediction of magnetization reversal driven by low-dimensional chaos induced by the RF drive [37]. However, this mechanism is expected to be

inactive in perfectly axially symmetric cylindrical structures with uniaxial magnetic anisotropy. This is because the dynamic system is effectively two-dimensional with one dimension represented by the magnetization polar angle and the other by the RF drive phase. According to the Poincaré – Bendixson theorem [53], such a system does not exhibit chaotic dynamics.

However, real nominally circular MTJ devices are known to deviate from this ideal picture and exhibit a weaker random in-plane uniaxial anisotropy in addition to the dominant out-of-plane uniaxial anisotropy [54, 55]. This anisotropy can arise from both the MTJ shape imperfections and from crystallographic anisotropy of the randomly oriented FL grains. In this case, both the polar and azimuthal angles of the magnetization enter the system's Lagrange function, and the RF drive makes the system effectively three-dimensional [56–58]. In such a system, RF-driven chaotic dynamics is expected above a threshold amplitude of the drive, and the threshold magnitude decreases with decreasing frequency. This RF-driven chaos mechanism can contribute to the observed RF assist and reduce the threshold for the onset of RF-induced switching over that theoretically predicted for ideal cylindrically-symmetric devices in Fig. 6.

In this work, we only made measurements of RF-assisted switching for random phase of the RF signal with respect to the onset of the DC write pulse. Our theoretical results in Fig. 6a,b suggest a route toward efficient RF-assisted switching in the regime of small overlap between the RF and DC pulses $\tau < 0$ when the phase of the RF signal is fixed. Indeed, the predicted switching probability in Fig. 6b shows switching probability enhancement nearing $\sim 50\%$ for 3 ns overlap of the RF and DC pulses. This is an order of magnitude larger than for the case of random RF pulse phase in Fig. 6d. While the RF-DC overlap regime may decrease the MTJ endurance, this decrease may be relatively small in some regimes of STT-MRAM operation, and the greatly increased switching probability may prove to be more important. This observation calls for future studies of the RF-assisted switching with fixed phase of the RF pulse.

Methods

Sample description The bottom electrode/ SAF/ MgO/ CoFeB(2.21 nm)/ top electrode multilayer stack was deposited by magnetron sputtering and patterned into circular MTJs using e-beam lithography and ion mill etching. Saturation magnetization of the CoFeB FL was determined by vibrating sample magnetometry, while its out-of-plane uniaxial magnetic anisotropy and Gilbert damping were determined by ST-FMR measurements (Supplementary Note 2) as summarized in Table I.

Spin torque ferromagnetic resonance We use ST-FMR to measure the frequency and linewidth of the FL spin wave modes as a function of out-of-plane magnetic field, and extract the FL Gilbert damping constant α and the uniaxial magnetocrystalline anisotropy constant

TABLE I. Material parameters of the MTJ CoFeB free layer: thickness, saturation magnetization M_s , uniaxial magnetocrystalline anisotropy constant K_{AN} , Gilbert damping constant α .

Quantity	Value	Unit
FL thickness	2.21	nm
M_s	1039	kA/m
K_{AN}	8.6×10^5	J/m ³
α	0.0097	

K_{AN} at room temperature from these data [59–61]. The values presented in Table I are an ensemble average of multiple devices. In these measurements, a microwave voltage is applied to an MTJ via the RF port of a bias tee. The applied voltage induces an RF spin transfer torque that excites spin waves in the FL and leads to oscillations of the sample resistance at the drive frequency due to tunneling magneto-resistance of the MTJ. These resistance oscillations mix with the RF current through the MTJ and generate a rectified DC voltage, which is measured by a lock-in amplifier through the DC port of the bias tee. The magnetic field modulation technique is employed to improve the signal-to-noise ratio [59].

RF-assisted switching probability measurements

Current-induced switching of the MTJ FL is observed by monitoring the change in the MTJ resistance in a circuit where the MTJ forms a voltage divider with a fixed resistor. We bias the voltage divider by a low-level DC voltage and use a 16-bit 2 MHz data acquisition board (DAQ) to measure time-dependent voltage across the MTJ. To

switch the FL, we apply a DC voltage pulse preceded by an RF voltage pulse to the MTJ. Details of the circuit and the waveform protocol are given in Supplementary Note 1. Following the RF+DC write waveform, we use DAQ to measure the resultant resistance state of the MTJ, which registers either switching or non-switching. A lower-amplitude, longer-duration DC reset pulse of the opposite polarity to the DC write pulse is then used to return the device to its initial state, and the DAQ is used to confirm the successful reset.

The RF pulse is generated by using a broadband microwave mixer connected to a microwave generator controlling the RF frequency and a square pulse generator controlling the output RF pulse duration. The amplitude of the RF pulse is controlled by both generators. All three pulse generators used in the measurements are synchronized with each other and the DAQ as described in Supplementary Note 1. The microwave generator operates in continuous wave mode, resulting in a random phase ϕ of the RF pulse. The delay τ between the RF and DC pulses is controlled through a combination of the cable length and a programmable internal delay of the DC write pulse generator. The switching probability \mathcal{P} is determined as a ratio of the number of successful switching events to the total number of switching attempts. The voltage levels of all RF+DC waveforms used in the measurements are characterized using a high-bandwidth real-time oscilloscope.

Data availability

All data generated or analyzed during this study are included in this published article and are available from the corresponding author on reasonable request.

-
- [1] G. E. Rowlands, T. Rahman, J. A. Katine, J. Langer, A. Lyle, H. Zhao, J. G. Alzate, A. A. Kovalev, Y. Tserkovnyak, Z. M. Zeng, H. W. Jiang, K. Galatsis, Y. M. Huai, P. Khalili Amiri, K. L. Wang, I. N. Krivorotov, and J.-P. Wang, *Applied Physics Letters* **98**, 102509 (2011).
- [2] H. Zhao, B. Glass, P. K. Amiri, A. Lyle, Y. Zhang, Y.-J. Chen, G. Rowlands, P. Upadhyaya, Z. Zeng, J. A. Katine, J. Langer, K. Galatsis, H. Jiang, K. L. Wang, I. N. Krivorotov, and J.-P. Wang, *J. Phys. D: Appl. Phys.* **45**, 025001 (2012).
- [3] M. Marins de Castro, R. C. Sousa, S. Bandiera, C. Ducruet, A. Chavent, S. Auffret, C. Pappas, I. L. Prejbeanu, C. Portemont, L. Vila, U. Ebels, B. Rodmacq, and B. Dieny, *Journal of Applied Physics* **111**, 07C912 (2012).
- [4] M. Cubukcu, O. Boule, N. Mikuszeit, C. Hamelin, T. Brächer, N. Lamard, M.-C. Cyrille, L. Buda-Prejbeanu, K. Garello, I. M. Miron, O. Klein, G. de Loubens, V. V. Naletov, J. Langer, B. Ocker, P. Gambardella, and G. Gaudin, *IEEE Transactions on Magnetism* **54**, 1 (2018).
- [5] T. Yamamoto, R. Matsumoto, T. Nozaki, H. Imamura, and S. Yuasa, *Journal of Magnetism and Magnetic Materials* **560**, 169637 (2022).
- [6] N. D. Rizzo, D. Houssameddine, J. Janesky, R. Whig, F. B. Mancoff, M. L. Schneider, M. DeHerrera, J. J. Sun, K. Nagel, S. Deshpande, H. Chia, S. M. Alam, T. Andre, S. Aggarwal, and J. M. Slaughter, *IEEE Transactions on Magnetism* **49**, 4441 (2013).
- [7] D. Apalkov, B. Dieny, and J. M. Slaughter, *Proceedings of the IEEE* **104**, 1796 (2016).
- [8] D. C. Worledge and G. Hu, *Nature Reviews Electrical Engineering* **1**, 730 (2024).
- [9] P. Khanal, B. Zhou, M. Andrade, Y. Dang, A. Davydov, A. Habiboglu, J. Saidian, A. Laurie, J.-P. Wang, D. B. Gopman, and W. Wang, *Applied Physics Letters* **119**, 242404 (2021).
- [10] K. Watanabe, B. Jinnai, S. Fukami, H. Sato, and H. Ohno, *Nature Communications* **9**, 663 (2018).
- [11] E. A. Montoya, J.-R. Chen, R. Ngelale, H. K. Lee, H.-W. Tseng, L. Wan, E. Yang, P. Braganca, O. Boyraz, N. Bagherzadeh, M. Nilsson, and I. N. Krivorotov, *Scientific Reports* **10**, 10220 (2020).
- [12] S. Sakhare, M. Perumkunnil, T. H. Bao, S. Rao, W. Kim, D. Crotti, F. Yasin, S. Couet, J. Swerts, S. Kundu,

- D. Yakimets, R. Baert, H. Oh, A. Spessot, A. Mouta, G. S. Kar, and A. Furnemont, in *2018 IEEE International Electron Devices Meeting (IEDM)* (2018) pp. 18.3.1–18.3.4.
- [13] W. Zhao, X. Zhao, B. Zhang, K. Cao, L. Wang, W. Kang, Q. Shi, M. Wang, Y. Zhang, Y. Wang, S. Peng, J.-O. Klein, L. A. De Barros Naviner, and D. Ravelosona, *Materials* **9**, 41 (2016).
- [14] N. Perrissin, S. Lequeux, N. Strelkov, A. Chavent, L. Vila, L. D. Buda-Prejbeanu, S. Auffret, R. C. Sousa, I. L. Prejbeanu, and B. Dieny, *Nanoscale* **10**, 12187 (2018).
- [15] I. M. Miron, K. Garello, G. Gaudin, P.-J. Zermatten, M. V. Costache, S. Auffret, S. Bandiera, B. Rodmacq, A. Schuhl, and P. Gambardella, *Nature* **476**, 189 (2011).
- [16] L. Liu, O. J. Lee, T. J. Gudmundsen, D. C. Ralph, and R. A. Buhrman, *Physical Review Letters* **109**, 096602 (2012).
- [17] S. Fukami, C. Zhang, S. DuttaGupta, A. Kurenkov, and H. Ohno, *Nature Materials* **15**, 535 (2016).
- [18] Y.-W. Oh, S.-h. Chris Baek, Y. M. Kim, H. Y. Lee, K.-D. Lee, C.-G. Yang, E.-S. Park, K.-S. Lee, K.-W. Kim, G. Go, J.-R. Jeong, B.-C. Min, H.-W. Lee, K.-J. Lee, and B.-G. Park, *Nature Nanotechnology* **11**, 878 (2016).
- [19] Q. Yang, D. Han, S. Zhao, J. Kang, F. Wang, S.-C. Lee, J. Lei, K.-J. Lee, B.-G. Park, and H. Yang, *Nature Communications* **15**, 1814 (2024).
- [20] V. Lopez-Dominguez, Y. Shao, and P. Khalili Amiri, *Journal of Applied Physics* **133**, 040902 (2023).
- [21] V. D. Nguyen, S. Rao, K. Wostyn, and S. Couet, *npj Spintronics* **2**, 48 (2024).
- [22] P. Baláz, M. Gmitra, and J. Barnaś, *Physical Review B* **79**, 144301 (2009).
- [23] E. Baek, I. Purnama, and C.-Y. You, *Physical Review Applied* **12**, 064004 (2019).
- [24] J. Z. Sun, *Physical Review B* **104**, 104428 (2021).
- [25] G. J. Kwiatkowski, M. H. Badarneh, D. V. Berkov, and P. F. Bessarab, *Physical Review Letters* **126**, 177206 (2021).
- [26] G. Finocchio, I. Krivorotov, M. Carpentieri, G. Consolo, B. Azzarboni, L. Torres, E. Martinez, and L. Lopez-Diaz, *J. Appl. Phys.* **99**, 08G507 (2006).
- [27] G. Finocchio, I. N. Krivorotov, X. Cheng, L. Torres, and B. Azzarboni, *Physical Review B* **83**, 134402 (2011).
- [28] X. Cheng, J. A. Katine, G. E. Rowlands, and I. N. Krivorotov, *Applied Physics Letters* **103**, 082402 (2013).
- [29] C. Thirion, W. Wernsdorfer, and D. Mailly, *Nature Materials* **2**, 524 (2003).
- [30] G. Woltersdorf and C. H. Back, *Physical Review Letters* **99**, 227207 (2007).
- [31] J.-G. Zhu, X. Zhu, and Y. Tang, *IEEE Transactions on Magnetics* **44**, 125 (2008).
- [32] H. T. Nembach, H. Bauer, J. M. Shaw, M. L. Schneider, and T. J. Silva, *Applied Physics Letters* **95**, 062506 (2009).
- [33] S. Okamoto, N. Kikuchi, M. Furuta, O. Kitakami, and T. Shimatsu, *Journal of Physics D: Applied Physics* **48**, 353001 (2015).
- [34] H. Suto, T. Nagasawa, K. Kudo, T. Kanai, K. Mizushima, and R. Sato, *Physical Review Applied* **5**, 014003 (2016).
- [35] Y.-T. Cui, J. C. Sankey, C. Wang, K. V. Thadani, Z.-P. Li, R. A. Buhrman, and D. C. Ralph, *Physical Review B* **77**, 214440 (2008).
- [36] S. H. Florez, J. A. Katine, M. Carey, L. Folks, O. Ozatay, and B. D. Terris, *Physical Review B* **78**, 184403 (2008).
- [37] E. A. Montoya, S. Perna, Y.-J. Chen, J. A. Katine, M. d'Aquino, C. Serpico, and I. N. Krivorotov, *Nature Communications* **10**, 543 (2019).
- [38] M. Carpentieri, G. Finocchio, B. Azzarboni, and L. Torres, *Physical Review B* **82**, 094434 (2010).
- [39] T. Taniguchi, D. Saida, Y. Nakatani, and H. Kubota, *Physical Review B* **93**, 014430 (2016).
- [40] H. Suto, T. Nagasawa, K. Kudo, K. Mizushima, and R. Sato, *Applied Physics Express* **8**, 023001 (2015).
- [41] T. McKinnon, B. Heinrich, and E. Girt, *Journal of Magnetism and Magnetic Materials* **546**, 168646 (2022).
- [42] C. Serpico, S. Perna, G. Bertotti, M. d'Aquino, A. Quercia, and I. D. Mayergoyz, *Journal of Applied Physics* **117**, 17A709 (2015).
- [43] I. Mayergoyz, G. Bertotti, and C. Serpico, *Nonlinear magnetization dynamics in nanosystems*, Elsevier Series in Electromagnetism (Elsevier Science, Amsterdam, 2009).
- [44] M. d'Aquino, S. Perna, and C. Serpico, *Physica B: Condensed Matter* **577**, 411744 (2020).
- [45] W. F. Brown, *Physical Review* **130**, 1677 (1963).
- [46] S. Amara-Dababi, H. Bea, R. Sousa, K. Mackay, and B. Dieny, *Journal of Physics D: Applied Physics* **45**, 295002 (2012).
- [47] E. Gapihan, J. Hérault, R. C. Sousa, Y. Dahmane, B. Dieny, L. Vila, I. L. Prejbeanu, C. Ducruet, C. Portemont, K. Mackay, and J. P. Nozières, *Applied Physics Letters* **100**, 202410 (2012).
- [48] L. Rehm, G. Wolf, B. Kardasz, E. Cogulu, Y. Chen, M. Pinarbasi, and A. Kent, *Physical Review Applied* **15**, 034088 (2021).
- [49] C. Safranski and J. Z. Sun, *Physical Review B* **100**, 014435 (2019).
- [50] I. Barsukov, Y. Fu, C. Safranski, Y.-J. Chen, B. Youngblood, A. M. Gonçalves, M. Spasova, M. Farle, J. A. Katine, C. C. Kuo, and I. N. Krivorotov, *Applied Physics Letters* **106**, 192407 (2015).
- [51] I. Barsukov, Y. Fu, A. M. Gonçalves, M. Spasova, M. Farle, L. C. Sampaio, R. E. Arias, and I. N. Krivorotov, *Applied Physics Letters* **105**, 152403 (2014).
- [52] Y.-J. Chen, H. K. Lee, R. Verba, J. A. Katine, I. Barsukov, V. Tiberkevich, J. Q. Xiao, A. N. Slavin, and I. N. Krivorotov, *Nano Letters* **17**, 572 (2017).
- [53] K. Ciesielski, *Central European Journal of Mathematics* **10**, 2110 (2012).
- [54] E. Hirayama, S. Kanai, K. Sato, M. Yamanouchi, H. Sato, S. Ikeda, F. Matsukura, and H. Ohno, *Japanese Journal of Applied Physics* **54**, 04DM03 (2015).
- [55] H. Mazraati, T. Q. Le, A. A. Awad, S. Chung, E. Hirayama, S. Ikeda, F. Matsukura, H. Ohno, and J. Åkerman, *Physical Review B* **94**, 104428 (2016).
- [56] C. Serpico, A. Quercia, G. Bertotti, M. d'Aquino, I. Mayergoyz, S. Perna, and P. Ansalone, *Journal of Applied Physics* **117**, 17B719 (2015).
- [57] O. J. Suarez, D. Laroze, J. Martínez-Mardones, D. Altbir, and O. Chubykalo-Fesenko, *Physical Review B* **95**, 014404 (2017).
- [58] A. M. Feron and R. E. Camley, *Physical Review B* **95**, 104421 (2017).
- [59] A. M. Gonçalves, I. Barsukov, Y.-J. Chen, L. Yang, J. A. Katine, and I. N. Krivorotov, *Applied Physics Letters* **103**, 172406 (2013).

- [60] C. J. Safranski, Y.-J. Chen, I. N. Krivorotov, and J. Z. Sun, *Applied Physics Letters* **109**, 132408 (2016).
- [61] I. Barsukov, H. K. Lee, A. A. Jara, Y.-J. Chen, A. M. Gonçalves, C. Sha, J. A. Katine, R. E. Arias, B. A. Ivanov, and I. N. Krivorotov, *Science Advances* **5**, eaav6943 (2019).

Acknowledgements

This work was primarily supported by Western Digital Technologies. Funding from the National Science Foundation via awards ECCS-2213690 and DMREF-2324203 as well as from the University of California National Laboratory Fees Research Program is also acknowledged. The authors thank the Eddleman Quantum Institute (EQI) for partial support of this work. S.P gratefully acknowledges financial support for this publication by the Fulbright Visiting Scholar Program, which is

sponsored by the U.S. Department of State and the Italian Ministry of Foreign Affairs and administered by the U.S. - Italy Fulbright Commission. Its contents are solely the responsibility of the author and do not necessarily represent the official views of the Fulbright Program, the Government of the United States, or the U.S. - Italy Fulbright Commission.

Author contributions

P.M.B., W.J. and C.D. made the samples. M.H. and I.N.K. designed the experiment. M.H. made the measurements. S.P., M.d'A. and C.S. developed the theoretical model. S.P. made numerical simulations. P.M.B and I.N.K. conceived the idea and supervised the project.

Competing interests

The authors declare no competing interests.

Supplementary Material
**Radio-frequency assisted switching in perpendicular magnetic
tunnel junctions**

Mark Hayward¹, Salvatore Perna², Massimiliano d'Aquino², Claudio Serpico²,
Wonjoon Jung³, Chunhui Dai³, Patrick M. Braganca³, and Ilya N. Krivorotov¹,

¹ *Department of Physics and Astronomy,*

University of California, Irvine, California 92697, USA

² *Department of Electrical Engineering and Information Technology,*

University of Naples Federico II, Naples, Italy. and

³ *Western Digital Technologies, San Jose, California, 95119, USA*

(Dated: December 16, 2025)

S1. RF-ASSISTED SWITCHING MEASUREMENT

We use the circuit in Fig. S1 to generate waveforms for current-induced switching of a magnetic tunnel junction (MTJ) free layer (FL), which consists of a combination of direct current (DC) and radio frequency (RF) pulses. Switching is detected by a change in MTJ resistance, monitored through a voltage divider formed with a fixed resistor R_{Ref} and the MTJ. We bias the voltage divider with a low-level DC voltage V_{Bias} and use a 16-bit 2 MHz data acquisition board (DAQ) to measure time-dependent voltage across the MTJ. To switch the FL, we first apply an RF voltage pulse to the MTJ followed by a DC voltage pulse from a Picosecond Pulse Labs 10,070A pulse generator. Following the RF+DC write sequence, we use the DAQ to measure the resultant MTJ resistance, which registers either switching or non-switching. Then Arbitrary Waveform Generator 2 sends a lower-amplitude, longer-duration DC reset pulse of opposite polarity to the DC write pulse to return the MTJ to its initial state, and the DAQ confirms a successful reset. The RF pulse is generated by using a broadband microwave mixer connected to a microwave generator, which controls the RF frequency, and to Arbitrary Waveform Generator 1, which controls the output RF pulse duration. The amplitude of the RF pulse is controlled by both generators. The RF,

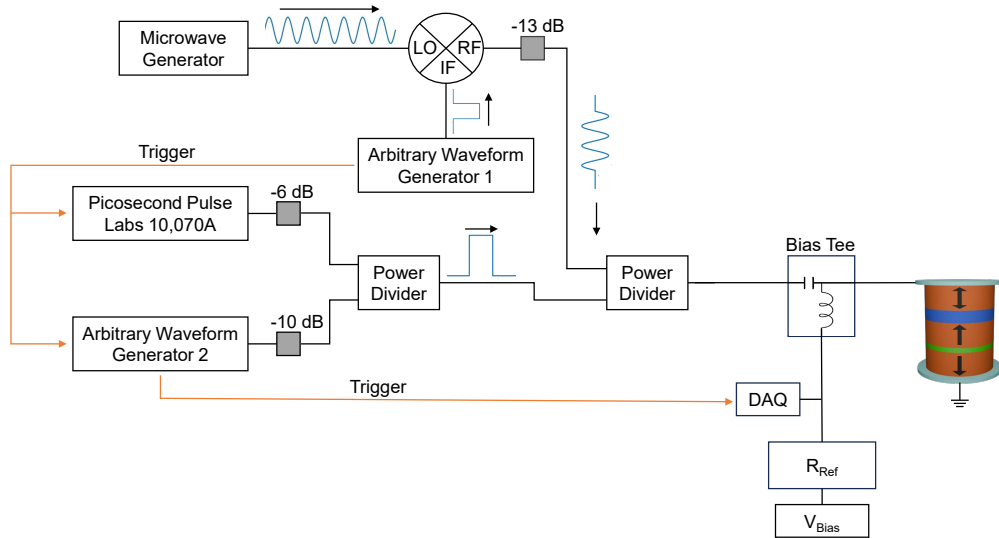


FIG. S1. Circuit diagram used to create combined RF-DC pulse waveforms.

DC write, and DC reset pulses are combined into one waveform via two power dividers. Attenuators placed throughout the circuit suppress the background signal from the mixer and protect the Picosecond Pulse Labs 10,070A output port from overloading.

The Picosecond Pulse Labs 10,070A and Arbitrary Waveform Generator 2 are triggered by the SYNC output of Arbitrary Waveform Generator 1. The DAQ is triggered by the SYNC output of Arbitrary Waveform Generator 2. The microwave generator operates in continuous wave mode, resulting in a random phase ϕ of the RF pulse. A delay τ between the RF and DC pulses is introduced and controlled by a combination of cable length and the programmable internal delay of the Picosecond Pulse Labs 10,070A. The switching probability \mathcal{P} is determined as a ratio of the number of successful switching events to the total number of switching attempts. Each measurement is repeated 10^5 times to reliably measure \mathcal{P} .

The pulse amplitudes of the RF+DC waveforms are characterized by replacing the MTJ in Fig. S1 with a high-bandwidth, real-time oscilloscope. However, because the oscilloscope has a $50\ \Omega$ input impedance, the scope does not account for the large impedance mismatch between the high impedance MTJ and the lower impedance circuit. This mismatch causes the pulse amplitudes delivered to the MTJ to nearly double in amplitude compared to the amplitude measured by the oscilloscope. The impedance mismatch and the subsequent increase in pulse amplitude must be taken into account during circuit calibration [1]. The root mean square (RMS) voltage of the RF pulse V_{RF} delivered to the high-impedance MTJ is given by Eq. (S1), where $V_{\text{PP}}^{\text{scope}}$ is the peak-to-peak voltage measured by the $50\ \Omega$ oscilloscope.

$$V_{\text{RF}} = \frac{2 \cdot V_{\text{PP}}^{\text{scope}}}{2\sqrt{2}} = \frac{V_{\text{PP}}^{\text{scope}}}{\sqrt{2}} \quad (\text{S1})$$

Similarly, Eq. (S2) gives the amplitude of the DC write and reset pulse dissipated by the high impedance MTJ. $V_{\text{DC}}^{\text{scope}}$ is the amplitude of the DC write pulse measured by the oscilloscope.

$$V_{\text{DC}} = 2 \cdot V_{\text{DC}}^{\text{scope}} \quad (\text{S2})$$

Equation (S3) defines RF power as the power dissipated by the sample (in dBm).

$$P_{\text{RF}} = 10 \cdot \log_{10} \left(\frac{V_{\text{RF}}^2}{R_{\text{P}}} \cdot \frac{1}{1\ \text{mW}} \right) \quad (\text{S3})$$

Here, V_{RF} is defined by Eq. (S1), and R_{P} is the resistance of the MTJ in the parallel resistance state. All pulse amplitudes reported in this work are the amplitudes dissipated by the MTJ as described by Eq. (S1) and Eq. (S2).

S2. SPIN TORQUE FERROMAGNETIC RESONANCE

We use spin torque ferromagnetic resonance (ST-FMR) to measure the frequency and linewidth of the free layer (FL) spin wave modes as a function of out-of-plane magnetic field. From these data, we extract the FL Gilbert damping constant α and the uniaxial magnetocrystalline anisotropy constant K_{AN} at room temperature [2–4]. In these measurements, a microwave voltage is applied to the MTJ via the RF port of a bias tee. The applied voltage applies an RF spin transfer torque that excites spin waves in the FL and leads to oscillations of the sample resistance at the drive frequency due to the tunneling magnetoresistance of the MTJ. These resistance oscillations mix with the RF current through the MTJ and generate a rectified DC voltage V_{mix} , which is measured by a lock-in amplifier through the DC port of the bias tee. The magnetic field modulation technique is employed to improve the signal-to-noise ratio [2]. The measured signal \tilde{V}_{mix} is proportional to the magnetic field derivative of the rectified DC voltage. The linewidth ΔH , defined as the half-width at half-maximum (HWHM) of the Lorentzian function, is obtained by fitting the resonance peaks to a sum of magnetic field derivatives of symmetric and anti-symmetric Lorentzian functions [2]. Figure S2a shows ST-FMR spectra for a $D = 85$ nm device, while Fig. S2b shows ΔH as a function of frequency. The data in Fig. S2b are fit using Eq. (S4) to extract the Gilbert damping constant α :

$$\Delta H(\omega) = \alpha \frac{\omega}{\gamma} + \Delta H(0) \quad (\text{S4})$$

where $\omega = 2\pi f$ is the microwave angular frequency, γ is the gyromagnetic ratio, and $\Delta H(0)$ is the frequency-independent linewidth due to the presence of magnetic inhomogeneities [5]. Figure S2c depicts frequency of the quasi-uniform (lowest frequency) spin wave mode as a function of magnetic field. The data points represent the resonance field for a given frequency extracted from Fig. S2a. Using the easy axis approximation of the Kittel equation, we fit Eq. (S5) to the data in Fig. S2 to determine the effective magnetic anisotropy H_K , from which the magnetocrystalline anisotropy constant K_{AN} is calculated:

$$\omega = \gamma (H + H_{\text{dip}} + H_K) \quad (\text{S5})$$

Here, H_{dip} is the center of the magnetic hysteresis loop, and the effective magnetic anisotropy is given by:

$$H_K = \frac{2K_{AN}}{\mu_0 M_s} - (D_z - D_{\perp}) M_s \quad (\text{S6})$$

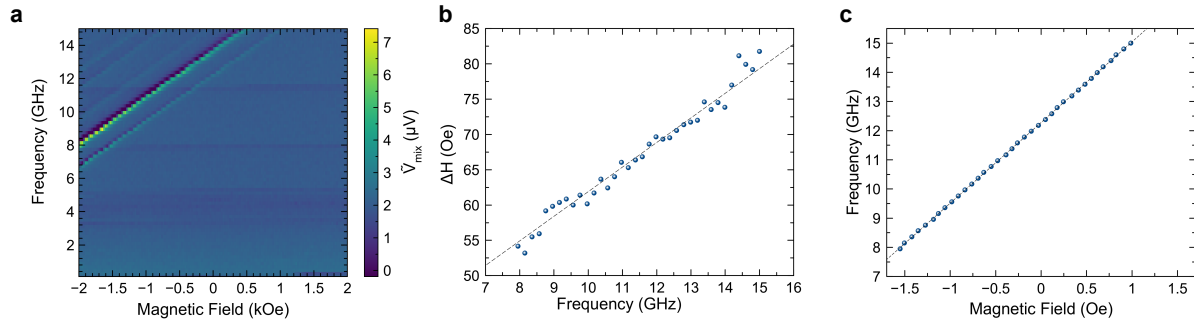


FIG. S2. **Spin torque ferromagnetic resonance measurements for a $D = 85$ nm device.** **a** \tilde{V}_{mix} as a function of frequency and magnetic field. **b** Linewidth ΔH defined as the HWHM of the resonance peak as a function of frequency fitted to Eq. (S4) **c** Frequency as a function of magnetic field where data points represent the resonance field for a given frequency fitted to Eq. (S5).

where M_s is the saturation magnetization, μ_0 is the magnetic permeability of free space, and D_z and D_\perp are the demagnetizing factor along the symmetry axis and perpendicular direction, respectively. These factors satisfy the relation: $2D_\perp + D_z = 1$ [5–7]. Fitting Eq. (S4) and Eq. (S5) to Fig. S2a,b respectively gives $\alpha = 0.0097$ and $K_{\text{AN}} = 8.2 \times 10^5 \text{ J/m}^3$.

S3. MICROMAGNETIC DESCRIPTION OF THE SWITCHING DYNAMICS

A. Micromagnetic model

The magnetization dynamics are described by the stochastic Landau-Lifshitz-Gilbert-Slonczewski (LLGS) equation expressed in the following normalized form [8]:

$$\frac{\partial \mathbf{m}}{\partial t} - \alpha \mathbf{m} \times \frac{\partial \mathbf{m}}{\partial t} = -\mathbf{m} \times \mathbf{h}_{\text{eff}} + \beta_{\text{ST}} \mathbf{m} \times (\mathbf{m} \times \mathbf{p}) - \nu \mathbf{m} \times \mathbf{h}_N, \quad (\text{S7})$$

where $\mathbf{m} = \mathbf{M}/M_s$ is the magnetic unit vector given by the ratio of the magnetization vector and the saturation magnetization at a given value of the absolute temperature T , t is the normalized time in units of $(\gamma M_s)^{-1}$ with γ being the absolute value of the gyromagnetic ratio, α is the Gilbert damping, $\mathbf{h}_{\text{eff}} = \mathbf{h}_{\text{ex}} + \mathbf{h}_{\text{m}} + \mathbf{h}_{\text{an}} + \mathbf{h}_{\text{a}}$ is the normalized effective field defined as the sum of the exchange, magnetostatic, anisotropy, and applied fields respectively, β_{ST} is the spin torque coefficient proportional to current, and \mathbf{p} is the magnetization unit vector of the polarizer.

The last torque term on the right-hand side is the stochastic torque acting on the magnetization field, where the coefficient ν satisfies the following fluctuation-dissipation relation: $\nu^2/(2\alpha) = k_B T/(\mu_0 M_s^2 V) = \tilde{T}$. Here, k_B is the Boltzmann constant and V is the volume of the free layer for macrospin simulations while it is the volume of the single cell for micromagnetic simulations. The thermal field $\mathbf{h}_N(t)$ is a Gaussian white noise whose components satisfy the following relations: $\langle h_{N,i}(t) h_{N,j}(t') \rangle = \delta_{ij} \delta(t - t')$, where the angular brackets $\langle . \rangle$ refer to the statistical average, δ_{ij} is the Kronecker delta and $\delta(t - t')$ is the Dirac delta function.

In the macrospin approximation, the magnetization is assumed to be spatially uniform. This produces zero exchange field. Moreover the magnetostatic field is assumed to be expressed by $\mathbf{h}_m = -\mathbf{D} \cdot \mathbf{m}$, where \mathbf{D} is a diagonal tensor ($\text{Tr}(\mathbf{D}) = 1$) whose components are the demagnetizing factors. Under the macrospin approximation, Eq. (S7) becomes an ordinary differential equation. In micromagnetic simulations, the magnetization of the free layer is, in general, not uniform, the exchange field is not zero, unlike the macrospin approximation, and the magnetostatic field depends on the magnetization field distribution by a nonlocal operator. The time-dependent excitation is simulated by giving β_{ST} the same time dependence of the voltage pulse waveform used in the experiments. The thermal field has been computed assuming the single replica is in contact with a thermal bath at room temperature $T = 300 \text{ K}$.

B. Analytic theory of switching probability

The discussion below establishes the theoretical basis for the analytical model and the assumptions (i)–(v) in the main text, presenting the explanations in order.

Numerical evidence supports the use of the macrospin model. More specifically, micromagnetic simulations agree quantitatively with ensemble simulations.

Stochastic magnetization dynamics can be described in probabilistic terms by writing the Fokker-Planck (FP) equation corresponding to the stochastic LLGS equation. When cylindrical coordinates are used and the FP equation is averaged along the azimuthal coordinate, the following equation is obtained [9]:

$$\frac{\partial p}{\partial t} = \frac{\partial}{\partial m_z} \left[\alpha(1 - m_z^2) \left(\frac{\partial \Phi}{\partial m_z} p + \tilde{T} \frac{\partial p}{\partial m_z} \right) \right], \quad (\text{S8})$$

where $p(m_z, t)$ is the probability density function (PDF) described in Eq. (5) in the main text, and $\Phi = k_{\text{eff}}/2(1 - m_z^2) + (\beta_{\text{ST}}/\alpha - h_{\text{az}})m_z$ is an effective potential that includes the magnetic free energy and the spin-torque effect. The term k_{eff} is the normalized effective magnetic anisotropy constant of the FL, and it is given by $k_{\text{eff}} = 2K_{\text{AN}}/(\mu_0 M_s^2) - (D_z - D_{\perp})$, where K_{AN} is the uniaxial magnetocrystalline anisotropy constant and D_z, D_{\perp} are the demagnetizing factors along the symmetry axis and the perpendicular direction.

Under the condition of stationary excitation, the distribution of the replicas will reach a steady state that is described by the following equilibrium PDF:

$$p_{\text{eq}}(m_z) = \frac{1}{Z} \exp\left(-\frac{\Phi}{\tilde{T}}\right), \quad m_z \in [-1, 1], \quad (\text{S9})$$

where $Z = \int_{-1}^1 \exp\left(-\Phi/\tilde{T}\right) dm_z$ is the partition function, and its value is such that the probability verifies the normalization condition: $\int_{-1}^1 p(m_z) dm_z = 1$. When the replicas are not distributed according to $p_{\text{eq}}(m_z)$, the PDF evolves according to a drift-diffusion process, where the ratio between k_{eff}/\tilde{T} gives us an indication about the character of the stochastic dynamics. In our case, $k_{\text{eff}}/\tilde{T} \gg 1$. This means that, when the external excitations are turned off, and all the replicas are in the well of one metastable state, relaxation towards the equilibrium PDF can be described by the Néel-Brown model in the high energy barrier case, with an initial distribution that is given by the following equation [9]:

$$p_0(m_z) = \frac{1}{Z} \exp\left(\frac{k_{\text{eff}}}{2\tilde{T}} m_z^2\right), \quad m_z \in [0, 1], \quad (\text{S10})$$

where in this case $Z = \int_0^1 \exp\left(\frac{k_{\text{eff}}}{2\tilde{T}} m_z^2\right) dm_z$.

Thermal relaxation to equilibrium occurs on a time scale that is much larger than the time window of the entire switching procedure (~ 100 ns). When the voltage overcomes the threshold value and the magnetic state of a certain replica moves far from its deterministic equilibrium, the PDF dynamics are driven mostly by the drift process and therefore the magnetization dynamics can be considered deterministic.

Ensemble simulations show that the switching probability does not change for $\tau \geq 0$. This result can be justified by investigating magnetization dynamics around the equilibrium. For $\tau \geq 0$, the RF voltage excites the system and the magnetic state moves far from equilibrium. However, the RF voltage is unable to switch the magnetic state on its own. When the RF voltage is turned off, a free evolution occurs around one of the two equilibria. When $\beta_{\text{ST}} > 0$, the time constant of the free evolution around the equilibrium can be

estimated to be: $\tau_E = (2\gamma M_s \alpha \omega_K)^{-1}$, where $\omega_K = k_{\text{eff}} + h_{az}$ is the dimensionless Kittel frequency. For $\beta_{\text{ST}} \sim 0.5 k_{\text{eff}}$, the time constant of the free evolution around equilibrium is $\tau_E \sim 1$ ns. However, experimentally we see influences of the RF voltage up to $\tau \approx 6$ ns. This suggests that the mechanism behind the increase in switching probability for $\tau \geq 0$ originates elsewhere. If magnetization nonuniformities are considered, the free evolution time constant for a generic spin wave mode of wave number k is $\tau_{Ek} = (2\gamma M_s \alpha \omega_k)^{-1} \sim 1$ ns, because $\omega_k \sim \omega_K$, where ω_k is the natural frequency of the k -th spin wave. This last consideration is also supported by numerical simulations (see main text), and it excludes the micromagnetic origin of the enhancement of switching probability for $\tau \geq 0$.

For $\tau < 0$, the RF voltage superimposes on the DC pulse, therefore $\beta_{\text{ST}} = \beta_{\text{DC}} + \beta_{\text{RF}}$. In a certain time window, the RF voltage can always be decomposed as $\beta_{\text{RF}} = \bar{\beta}_{\text{RF}} + \delta\beta_{\text{RF}}(t)$, where $\bar{\beta}_{\text{RF}}$ is the average value of the RF voltage on the DC pulse time window. If the RF power is small compared to the DC power, $|\beta_{\text{DC}} + \bar{\beta}_{\text{RF}}| \gg |\delta\beta_{\text{RF}}(t)|$, the equation governing the dynamics of m_z can be then written as:

$$\alpha k_{\text{eff}} dt = \frac{dm_z}{(1 - m_z^2)(m_z - H(t))} \approx \frac{dm_z}{(1 - m_z^2)(m_z - \bar{H})}, \quad (\text{S11})$$

where $H(t) = \beta_{\text{ST}}(t)/(\alpha k_{\text{eff}})$ and $\bar{H} = (\beta_{\text{DC}} + \bar{\beta}_{\text{RF}})/(\alpha k_{\text{eff}})$ is the effective DC voltage pulse amplitude normalized to the critical DC voltage for switching at zero temperature in dimensionless units. This argument also explains why for high RF power the analytical estimation of the probability is not accurate anymore.

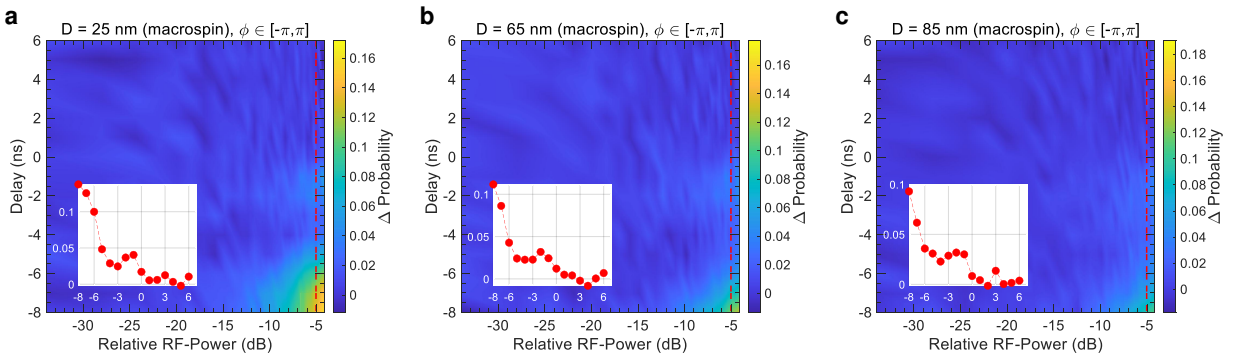


FIG. S3. Change of switching probability as a function of of normalized RF power \tilde{P}_{RF} and delay τ , with random phase $\phi \in [-\pi, \pi]$. **a** $D = 25$ nm. **b** $D = 65$ nm. **c** $D = 85$ nm.

C. Switching probability: additional figures

In Fig. S3, the change in switching probability is shown as a function of normalized RF-power \tilde{P}_{RF} – defined relative to the minimal theoretical power required to switch the magnetic state with a DC current in the absence of thermal fluctuations ($T = 0$ K) – and the delay τ of the DC pulse with respect to the RF pulse for $\phi \in [-\pi, \pi]$ and multiple device diameters. The diagrams look qualitatively similar; in particular, lower delay τ and higher relative power show higher enhancement of switching probability.

REFERENCES

- [1] D. M. Pozar, in *Microwave engineering* (Wiley, Hoboken, NJ, 2012) 4th ed., pp. 85–90.
- [2] A. M. Gonçalves, I. Barsukov, Y.-J. Chen, L. Yang, J. A. Katine, and I. N. Krivorotov, [Applied Physics Letters](#) **103**, 172406 (2013).
- [3] C. J. Safranski, Y.-J. Chen, I. N. Krivorotov, and J. Z. Sun, [Applied Physics Letters](#) **109**, 132408 (2016).
- [4] I. Barsukov, H. K. Lee, A. A. Jara, Y.-J. Chen, A. M. Gonçalves, C. Sha, J. A. Katine, R. E. Arias, B. A. Ivanov, and I. N. Krivorotov, [Science Advances](#) **5**, eaav6943 (2019).
- [5] B. Heinrich and J. Cochran, [Advances in Physics](#) **42**, 523 (1993).
- [6] C. Kittel, [Physical Review](#) **73**, 155 (1948).
- [7] M. Beleggia, M. D. Graef, and Y. T. Millev, [Journal of Physics D: Applied Physics](#) **39**, 891 (2006).
- [8] I. Mayergoyz, G. Bertotti, and C. Serpico, *Nonlinear magnetization dynamics in nanosystems*, Elsevier Series in Electromagnetism (Elsevier Science, Amsterdam, 2009).
- [9] W. F. Brown, [Physical Review](#) **130**, 1677 (1963).